Study of the circularity effect on drag of disk-like particles

L.B. Esteban[a], J. Shrimpton[a,*], B. Ganapathisubramani[a]

[a] *University of Southampton, Faculty of Engineering and Physical Sciences, Highfield Road, Southampton, UK*

Abstract

This paper presents a study of the terminal fall velocity, drag coefficient and descent style of 'wavy-edge' flat particles. Being highly non-spherical and with a size of up to a few centimetres, these particles show strong self-induced motions that lead to various falling styles that result in distinct drag coefficients. This study is based on experimental measurements of the instantaneous 3D velocity and particle trajectory settling in water. A disk of $D = 30\,\mathrm{mm}$, $t = 1.5\,\mathrm{mm}$ and $\rho = 1.38\,\mathrm{g/cm^3}$ is manufactured as a reference particle. The disk was initially designed to lie within the Galileo number - dimensionless moment of inertia ($G - I^*$) domain corresponding to the fluttering regime. A total of 35 other particles with the same frontal area and material properties were manufactured. These are manufactured to have different amplitudes (a) of the sinusoidal wave on the edge and number of cycles (N) around the entire perimeter. Thus, 5 sets of particles are manufactured with different relative wave amplitudes; i.e. $a/D = 0.03$, 0.05, 0.1,

*Corresponding author

Email addresses: lbe1g14@soton.ac.uk (L.B. Esteban), john.shrimpton@soton.ac.uk (J. Shrimpton), g.bharath@soton.ac.uk (B. Ganapathisubramani)

0.15, 0.2. Each set consisting of 7 particles from $N = 4$ to $N = 10$. The isoperimetric quotient is used as a measure of the particle circularity and is also linked with different characteristic settling behaviours. Disks and other planar particles with small a/D ratio were found to descent preferably with 'Planar zig-zag' behaviour with events of high tilted angle. In contrast, particles with high a/D ratio were found to follow a more uniform descent with low tilted angle to the vertical motion. The differences in projected frontal area were shown not to be sufficient to compensate the differences in descent velocity, leading to unequal drag coefficients. Therefore, we believe that the falling styles of these irregular particles go hand by hand with characteristic wake structures, as shown for disks with various dimensionless moment of inertia, that enhance the descent of particles with low circularity.
Keywords: Drag Coefficient, Irregular particle, Settling, Circularity

1. Introduction

The motion of particles in a viscous continuum appears in many industrial applications; from pneumatic conveyors in the food industry to pulverized-fuel boilers in the generation of thermal energy. It is in the design and modelling processes of such facilities when the size, shape and subsequent fluid dynamic effects of the solid particles gain importance, since these are directly linked to key features such as dispersion and the heat transfer rate. Although industrial facilities deal with a large number of solid characteristics, the understanding of the effect of shape of these particles on their trajectory is limited.

The motion of freely falling non-spherical particles is complex, even for

relatively simple geometries such as disks. These particles show a variety of falling regimes that go from steady fall to tumbling, through fluttering and chaotic motion. The first phase diagram showing the falling scenarios of a disk was defined by Willmarth et al. (1964) in the Reynolds number (Re) and the dimensionless moment of inertia (I^*) domain. The Reynolds number defined as $Re = V_z D/\nu$, where V_z is the average settling velocity, D is the diameter of the disk and ν is the kinematic viscosity of the fluid. The dimensionless moment of inertia as $I^* = I_p/\rho_f D^5$, where I_p is the moment of inertia about the diameter of the disk and ρ_f is the density of the fluid. They carried out a series of experiments and mapped the different falling regimes they observed: steady, fluttering and tumbling. They discussed that the phase diagram held for disks, as long as the aspect ratio (χ) defined as $\chi = D/h$ was large (where h is the thickness of the disk).

Field et al. (1997) identified a new falling regime within the phase diagram defined by Willmarth et al. (1964) between flutter and tumbling regimes. This new regime was labelled as 'Chaotic' and has been investigated in more detail during the past decades, especially for two-dimensional rectangular plates; Belmonte et al. (1998), Andersen et al. (2005b) and (Andersen et al., 2005a).

Zhong et al. (2011) focused on thin disks ($\chi \geq 10$) and showed experimentally that the trajectory of a disks transitions from 'Planar zig-zag' to 'Spiral' motion for a region in the phase diagram associated with fluttering motion. They showed that this transition is determined by the relative particle to fluid inertia (I^*). They also carried flow visualization and showed that the change in path style comes with a drastic change in the turbulent

structures present in the wake. They discussed that the transition between these three sub-regimes, i.e. 'Planar zig-zag', 'Transitional' and 'Spiral', is Reynolds number dependent. They also showed that this phenomenon was not sensitive to initial tilt. Lee et al. (2013) extended the work of Zhong et al. (2011) by doing planar Particle Image Velocimetry measurements on the particle wake. They found that disks with moderate inertia followed a 'Planar zig-zag' motion and with decreasing I^* the particles transitioned to a 'Spiral' motion.

On the other hand, numerical investigations on the falling styles of disks have shed light on the descend mechanisms at low to moderate Re numbers. Auguste et al. (2013) carried out a thorough numerical investigation on the dynamics of thin disks falling under gravity in a viscous fluid medium at $Re < 300$ and found two new three-dimensional paths in which the plane of motion slowly rotates about the vertical axis. Similarly, Chrust et al. (2013) performed direct numerical simulations of the solid-fluid interactions of infinitely thin disks and presented a parametric study on the effect of the Galileo number ($G = \sqrt{|\rho_p/\rho_f - 1|gD^3}/\nu$), which is an alternate form of Re, and the non-dimensional mass (m^*), being $m^* = \frac{m}{\rho_f D^3}$. They also studied 'three-dimensional states' and found similar falling styles for disks with $I^* = 3.12 \times 10^{-3}$ and $Re = 320$ as reported in Auguste et al. (2013), Zhong et al. (2011) and Lee et al. (2013). They showed that the saturated 'Spiral' state was reached after a fall distance of $\approx 60\,D$. The distance travelled by the disk to reach the 'Spiral' state greatly differs between studies, suggesting that not only the dimensionless moment of inertia but the Reynolds number affects the duration of the transient effects. Similarly, Zhou et al. (2017) performed

direct numerical simulations for freely falling oblate spheroids with aspect ratios $1 < \chi < 10$. They also found that several drastically different descent modes coexist for the same parameter space. This shows that the falling motion of these particles is not unique and therefore should be examined through statistical analysis.

Fewer studies are available for planar non-spherical particles other than disks or rectangular plates. In the early 70's, List and Schemenauer (1971) investigated the steady fall of different shapes including hexagonal plates, broad-branched crystals, dendrites and stellar crystals. In addition to variation of drag coefficient (C_D) with Reynolds number (due to viscous effects), small oscillations in the fall trajectories of hexagonal plates and broad-branched models were observed. These oscillations were reported to be smaller than those of circular disks with the same frontal area, but no quantitative measurements were taken. Jayaweera (1972) studied experimentally the free fall behaviour of various planar particles within the same range of Reynolds number ($Re < 50$). These planar particles were manufactured with the same frontal area and thickness of a reference disk for comparison. They showed that the terminal velocity of hexagonal plates was practically the same of the equivalent disk while for the case of star-shape particles the differences in the terminal velocity were up to 25%. However, the severe difference in the viscous effect ($Re < 50$) associated with increasing the particle perimeter was considered to be the only mechanism responsible for the change in the particle descent velocity. Kajikawa (1992) studied the free-fall patterns and the variation in the vertical and horizontal velocities of "snow crystal shapes". They found a very small fluctuation in the settling velocity

for all particles investigated, which suggests that they were close to the stable fall regime. They also found that dendritic crystals with large internal ventilation fall with a stable pattern over a larger Re range compared to simple hexagonal plates. This suggests that the stability of the falling motion was influenced by the internal ventilation of the crystals, as confirmed later by Vincent et al. (2016) for disks. More recently, Maggi (2015) showed how fractal structures can modify the resistance of granular aggregates moving through water whereas Bagheri and Bonadonna (2016) presented a comprehensive analytical and experimental investigation on the drag coefficient of non-spherical particles, where particle secondary motion, the effect of particle orientation and the effect of particle-to-fluid density ratio on the drag coefficient were discussed. Also, several polygonal shapes have been recently investigated through water tank experiments in (Esteban et al., 2018); showing the edge effect on the descent style of these particles.

Despite these isolated studies on the frontal geometry effect on the descent velocity, there is still a lack of understanding on when a flat particle originally falling under fluttering motion transitions to a more stable regime due to changes in frontal geometry. Similarly, it is not known if the effect of the effective particle projected area under these new conditions is the reason for the change in drag coefficient.

Therefore we propose to study the effect of the gradual change in the perimeter geometry (from disks to particles with very low circularity) on the particle trajectory. This will also tackle one of the questions suggested in Moffatt (2013) regarding the dynamics of disks: the effects of the perimeter geometry on the settling characteristics of flat irregular particles moving in

a viscous media. In here we include the effect on the particle dispersion, the mean and instantaneous descent velocity, and the types of secondary motion that are directly linked to particle orientation and therefore drag coefficient.

2. Methods

In order to investigate how the waviness of the perimeter affects the settling dynamics of the disk, we manufactured a reference disk with a diameter $D = 30\,\mathrm{mm}$, thickness $h = 1.5\,\mathrm{mm}$ and density $\rho = 1.38\,\mathrm{g/cm^3}$ that falls in the fluttering regime with a Reynolds number $Re \approx 1800$ and non-dimensional inertia $I^* = 3.4 \times 10^{-3}$. Then, keeping the disk thickness (h) and frontal area A constant we vary the amplitude of the sinusoidal wave on the edge (a) and the number of cycles, or peaks, around the entire perimeter (N), as sketched in figure 1. Thus, we manufactured 5 sets of particles with different relative wave amplitudes; i.e. $a/D = 0.03$, 0.05, 0.1, 0.15, 0.2, each set consisting of 7 particles from $N = 4$ to $N = 10$ with the corresponding dimensionless moment of inertia shown in table 1. The parameter space (a/D, N) is chosen to cover a wide geometric range. As these two parameters increase, the particle becomes less similar to a disk and more like a star-shape particle. The combined effect of these parameters can be also seen from a circularity point of view. In here, the isoperimetric quotient ($Q = 4\pi A/P^2$) is the parameter used to characterize geometric changes, shown in brackets in table 2. The hypothesis is that as a/D and N increases (and therefore Q), the characteristic fluttering motion of the solid disks becomes less pronounced as discussed in Kajikawa (1992) for particles with inner ventilation.

	N						
a/D	4	5	6	7	8	9	10
0.03	2.5	2.5	2.5	2.5	2.5	2.5	2.5
0.05	2.1	2.1	2.1	2.1	2.1	2.1	2.1
0.1	1.5	1.5	1.5	1.5	1.5	1.5	1.5
0.15	1.1	1.1	1.1	1.1	1.1	1.1	1.1
0.2	0.94	0.94	0.94	0.94	0.94	0.94	0.94

Table 1: Dimensionless moment of inertia ($I^* \times 10^3$) based on the diameter of the circumscribed disk.

All particles were laser cut within a precision of $\pm 0.5\,\mathrm{mm}$. Table 2 shows the length of the perimeter of the particles manufactured, whereas table 3 summarizes the mass of the particles after the manufacture process was completed. Small differences in the mass of the particles were caused by the addition of black paint (to facilitate the image treatment).

In water, the particles were released from about $2\,D$ below the surface so that entry and surface effects were avoided. The particles were released with zero initial velocity and zero tilted angle using a release mechanism that used active suction. All particles were held in their initial position by a suction cup smaller than their internal diameter. The suction cup was part of a rigid frame attached to the water tank, ensuring that the particle initial conditions were the same in all realizations. The water tank was $0.8\,\mathrm{m}$ high with a cross-section of $0.5\,\mathrm{m} \times 0.5\,\mathrm{m}$. All particles used were made of polyester with a

	N						
a/D	4	5	6	7	8	9	10
0.03	96(0.97)	96(0.96)	97(0.94)	98(0.92)	100(0.90)	101(0.87)	102(0.85)
0.05	98(0.93)	100(0.89)	102(0.85)	105(0.81)	108(0.76)	111(0.72)	115(0.68)
0.1	108(0.76)	115(0.68)	122(0.59)	131(0.52)	139(0.46)	149(0.40)	158(0.36)
0.15	122(0.59)	135(0.49)	149(0.40)	163(0.33)	178(0.28)	194(0.24)	210(0.20)
0.2	139(0.46)	158 (0.36)	178(0.28)	199(0.22)	220(0.18)	242(0.15)	264(0.13)

Table 2: Particle perimeter (P) in millimeters for shapes with same area to a disk with $P = 94.2$ mm. Isoperimetric quotient Q is represented in brackets

density of approximately $1.38\,\mathrm{g/cm^3}$, frontal area of $7.07\,\mathrm{cm^2}$ and a thickness of $1.5\,\mathrm{mm}$.

Two cameras were used to capture the falling particle. One camera captured a frontal view of the descent motion of the particle while the other captured the planar $(X - Y)$ motion of the particle through a mirror at 45° underneath the tank. The cameras were both focused on the mid-plane of the tank to minimize image distortion. The trajectories were recorded at $60\,\mathrm{fps}$. This frame-rate was sufficient to resolve the translational motion during all parts of the descent to within $2\%D$. A diffused light source was used to back illuminate the water tank. In each frame the dark particle projection was recorded onto the white background and the position of the centre of mass of the particle was obtained by locating the geometric centre of each particle projection. As discussed in Esteban et al. (2018), the shadow of the particle can hide individual peaks during the fall, leading to an erroneous location of

	N						
a/D	4	5	6	7	8	9	10
0.03	1.50	1.50	1.49	1.50	1.51	1.50	1.48
0.05	1.50	1.49	1.49	1.48	1.47	1.51	1.50
0.1	1.52	1.51	1.50	1.50	1.50	1.50	1.50
0.15	1.58	1.57	1.57	1.54	1.55	1.53	1.54
0.2	1.63	1.64	1.63	1.60	1.60	1.59	1.59

Table 3: Particle Mass in grams.

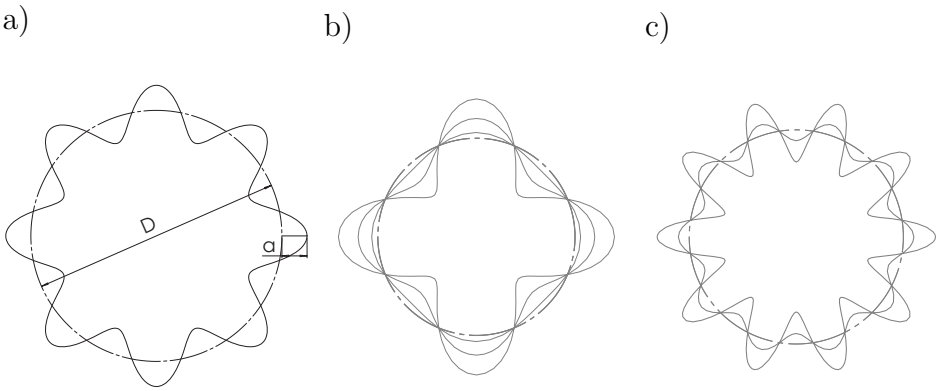

Figure 1: a) Sketch of a 'wavy-edge' particle about the reference disk perimeter; b) Wavy-edge particles with constant $N = 4$ and $a/D = 0.2$, 0.1, 0.03; c) Wavy-edge particles with constant $N = 10$ and $a/D = 0.15$, 0.05.

the center of gravity (only in the Z component for this camera arrangement) and could be maximum for the $N = 5$, $a/D = 0.2$ particle ($\pm 0.05\, D$). This is only relevant for particles with an odd number of peaks when they have a symmetry plane parallel to the camera focal plane. Also, the particle has to be at a high incidence angle for this effect to be noticeable. These conditions make this specific particle alignment extremely rare and we do not observe any bias in the results due to this potential measurement error. However, the measured trajectories were smoothed with a polynomial filter of 3rd order and frame length of 5 points to filter out high frequency noise from this and other measurement errors.

A set of releases for a sphere falling in air was performed to establish limitations on the accuracy associated with the suction mechanism as well as the camera alignment and account for image distortion from the lens. The variance in the landing position was interpreted as the uncertainty of the complete system. This was found to be two orders of magnitude smaller than the sphere diameter. This is in accordance with the uncertainty typically found in the literature for similar drop mechanisms, (Heisinger et al., 2014). The method followed to obtain the particle centre of mass from the raw images did not add any uncertainty.

To build a baseline from which to compare the motion of the 'wavy-edge' particles a first set of 50 repeated drops of the disk in water was performed. All trajectories were recorded prior to their release instant. The determination of the distance at which the particle motion is not influenced by the initial transient dynamics is non-trivial. Chrust et al. (2013) performed simulations of an infinitely thin disks with $I^* = 3.12 \times 10^{-3}$ and $G = 300$ and

showed that it reached a saturated path at a vertical distance of $\approx 60\,D$ from the release point, whereas Heisinger et al. (2014) showed experimentally that for disks with $I^* \approx 3 \times 10^{-3}$ and $G \approx 4180$, the disk trajectory was saturated after a distance of $7\,D$. Here the reference disk lies closed to the parameter space in Heisinger et al. (2014), with $I^* = 3.4 \times 10^{-3}$ and $Re \approx 1800$. We also found that the disk and other particles with small a/D ratios showed a saturated state at a distance of $7\,D$, whereas for larger a/D ratios this distance was reduced. Thus, a distance of $7\,D$ is given to the particle to accommodate to the fall before the trajectories are analysed. This is consistent with the distance found in Esteban et al. (2018) for disks and other n-polygon planar particles lying in a similar location in the $Re - I^*$ domain.

As discussed in Esteban et al. (2018), the bottom of the tank influences the landing position of the particle not only due to hydrodynamic interactions but because the particle slides over the glass surface after the impact. To overcome these influences we do not process the particle trajectory once it reaches a distance of $2\,D$ from the bottom of the tank. The method to discard the last section of the trajectory is the following: we use the images recorded by the top camera (frontal view of the descent) to monitor the vertical position of the particle and when it reaches the desired vertical location; i.e. $2\,D$ from the bottom, we save the specific frame number. Then, when we read the frames from the bottom camera to find the particle $X - Y$ position we stop the analysis at the frame number previously saved. Thus, we now have a trajectory section that goes from $7\,D$ from the top (corresponding to a location were the particle trajectory is at a saturated state) to $2\,D$ from the bottom (unperturbed by the glass surface). This trajectory section

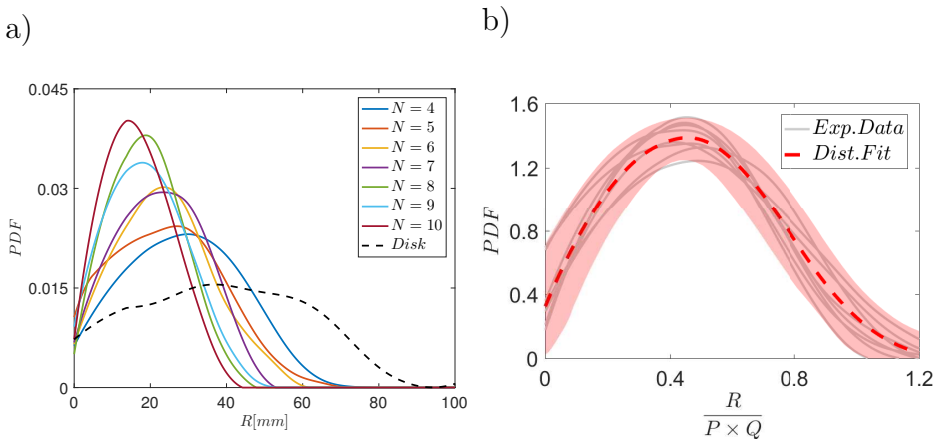

Figure 2: a) Probability density function of finding an $a/D = 0.2$ particle with variable N at a certain radial distance (R) from the release point. b) Probability density function of finding a particle at a radial distance normalized with the particle diameter and the isoperimetric quotient. Data taken at $z > 7D$

corresponds to $\approx 15\,D$ and at least 7 particle periods.

Each particle is released 50 times in water at room temperature, $\rho_f = 0.998\,\mathrm{g/cm^3}$ and $\nu = 1.004 \times 10^{-6}\,\mathrm{m^2/s}$, the waiting time between drops being of 20 min, corresponding to more than 600 times the particle time-scale of the oscillatory motion.

3. Results

3.1. Planar dispersion, normal to the descent direction.

The raw radial dispersion of particles with $a/D = 0.2$ and variable N together with the radial dispersion of the reference disk is shown in figure 2 a). The radial distribution of the disk is the broadest of all particles tested, having its mean value at about 45 mm from the origin ($\approx 1.5\,D$). Then, as the isoperimetric quotient of the particle reduces, the radial dispersion of the

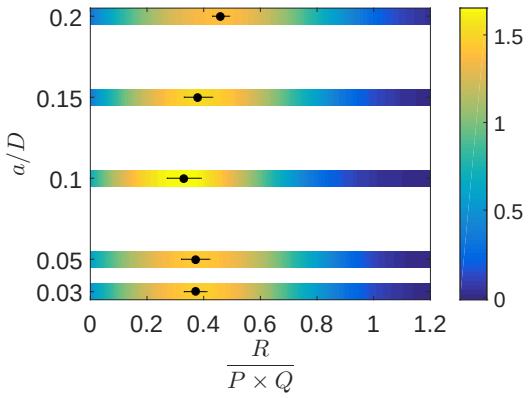

Figure 3: Contour plots of the probability density functions of finding a particle of a given family (a/D) at a radial distance normalized with the particle diameter and the isoperimetric quotient. The solid dot represents the peak of the contour plot and the horizontal line the dispersion on the peak location from particles with variable N

particles becomes narrower, with particles of $N = 10$ having its mean value at about 17 mm from the origin ($\approx 0.5\,D$). Figure 2 b) shows a collapse of the statistics for the probability of finding a particle at a given radial distance from the origin once the perimeter of the particle (P) and the isoperimetric quotient (Q) are considered. The family of particles with $a/D = 0.2$ is chosen for representation since these are the particles characterized by the smaller circularity. This result suggests that the amplitude of the planar oscillations are not only dependent on the particle perimeter but also on the frontal geometry (here defined by the isoperimetric quotient). Thus, Q is the correct parameter to make radial dispersion self similar with perimeter shape. The same approach is followed for all a/D families of particles and the contours of the probability density functions are shown in figure 3. The peaks of the distributions are represented with a solid dot, whereas the uncertainty on the peak location coming from the dispersion of the results for different particles

within the same family is represented with solid lines. The evolution of the peak location suggests that this normalization on the radial dispersion might overcompensate the results for the case of very irregular particles ($a/D > 0.2$), since it starts to deviate from the nearly constant value of 0.4 for $a/D \leq 0.15$.

3.2. Secondary motion

The differences observed in the particle planar dispersion suggest that these might exhibit different secondary motions depending on the characteristics of the particle perimeter. In this section, individual particle trajectories are plotted and compared to identify the main differences between geometries. Figure 4 shows trajectory samples of different particles, where maximum and minimum velocity events are shown with solid and empty dots respectively.

From the inspection of these trajectories one can observe that the disk, figure 4 a) and figure 5 a) , describes a zig-zag motion that is approximately contained in a single plane of motion. We observe that as the number of waves around the perimeter increases the particle gains more out-of-plane motion, leading to a quasi-spiral motion for the case seen in figure 4 c) and 5 c). There is another new type of trajectory in between these two clearly different styles of descent that remains stable for the length of the trajectories recorded. This type of descend is in fact a mixture of the zig-zag and quasi-spiral motion (figure 4 b)), with the velocity in the $X - Y$ plane being a combination of angular and linear velocity. This leads to the characteristic descent footprint shown in figure 5 b), where the particle

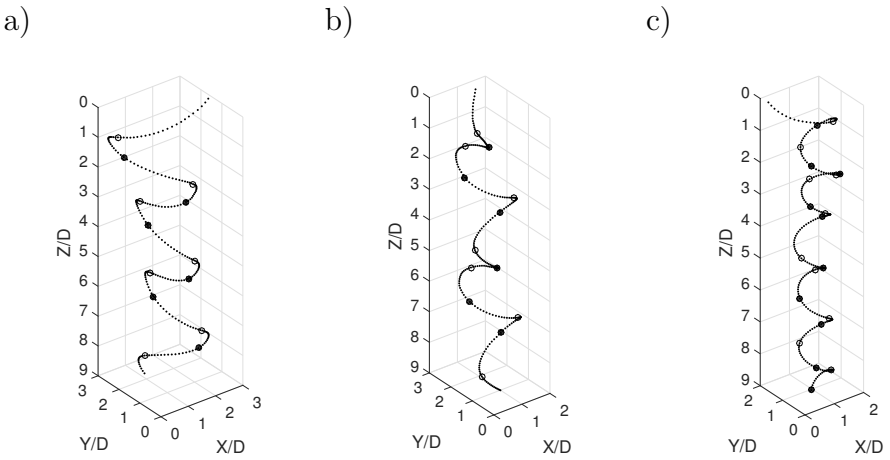

Figure 4: 3D trajectory sections of the reconstructed particle fall: a) Disk, b) planar particle with $a/D = 0.2$ and $N = 6$, c) planar particle with $a/D = 0.2$ and $N = 10$. Solid and empty dots represent events of maximum and minimum descent velocity respectively.

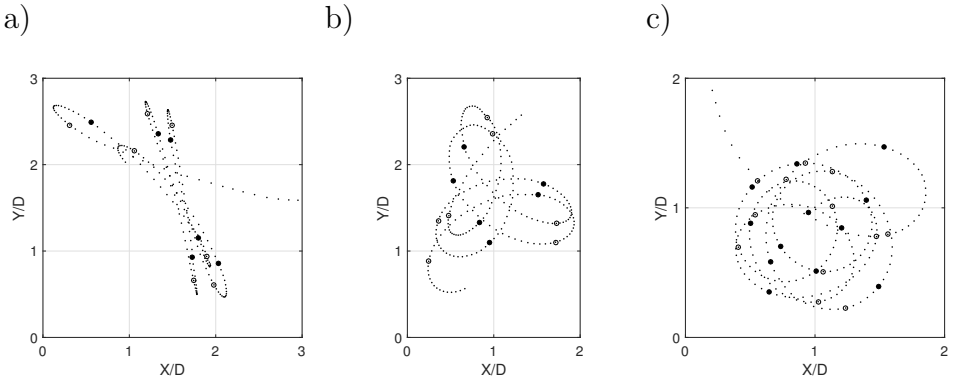

Figure 5: $X - Y$ trajectory sections of the reconstructed particle fall shown in figure 4. Solid and empty dots represent events of maximum and minimum descent velocity respectively.

trajectory in the $X - Y$ plane resembles a rhodonea curve, as shown in Zhong et al. (2011) for disks with small dimensionless moment of inertia I^*. Minimum and maximum descent velocity events appear at the same relative locations for the trajectory types of figure 4 a) and b), with the turning trajectory section being always bounded in between a minimum and maximum descent velocity event. In contrast, quasi-spiral trajectories; as in 4 c), do not show this clear distribution of fast and slow events in favour of a less organized arrangement of minimum and maximum descent velocity events. Thus, in the following sections we investigate if the various descent styles observed are associated with differences in descent velocity, particle orientation and drag coefficient.

3.3. Descent Velocity and Drag Coefficient

Results from the particle planar dispersion and particle secondary motion show strong differences in the settling characteristics of planar irregular particles. In this section, the descent velocity associated with the different falling styles observed is investigated. A mean descent velocity per trajectory is obtained from $7\,D$ to the release point to $2\,D$ from the bottom ($\approx 15D$), corresponding to at least 7 periods of oscillation. Then, a unique descent velocity per particle geometry is obtained as the mean of 50 realizations. The results from the descent velocity can be used to obtain the Reynolds number of the particles, see table 4, that allow us to locate them in the $Re - I^*$ phase diagram of disks. It is interesting to note that when the diameter of the circumscribed disk is taken as a characteristic length scale of the particle, the results regarding the particle secondary motion agree well with their location in the phase diagram as shown in figure 6. Thus, as a/D increases (and

therefore I^* decreases) the falling style of the particle transitions towards the helical motion.

Figure 7 a) shows the variation of the measured mean terminal velocity (V_z) of all planar particles considered in this study. The mean terminal velocity is shown relative to that of the circular disk ($\tilde{V_z} = V_z/V_{z_{disk}}$). The mean terminal velocity is plotted as a function of the number of peaks (N) around the perimeter. The standard deviation from the 50 realizations is below 10% for all geometries investigated and it is not shown to help the figure visualization. The experimental data shows that particles with $N = 4$ and small a/D ratio; i.e. $a/D = 0.03$, $a/D = 0.05$ and $a/D = 0.1$, have a descent velocity that is slightly higher than the reference disk descent velocity. Also, there is a consistent increase in descent velocity for these families of particles as the number of peaks (N) around the perimeter increases. On the other hand, the decent velocity of the families with $a/D = 0.15$ and $a/D = 0.2$ lies below the disk descent velocity for $N = 4$ but rapidly increases, exceeding the descent velocity values of the particles with small a/D ratios for $N > 7$.

The Drag Coefficient combines the mean descent velocity with the mass of the particle and the particle projected area to give a more robust comparison between perimeter shapes than figure 7 a). The Drag Coefficient based on the projected area is of particular interest in this study because of the following reason: all particles share the same frontal area; however, when falling in quiescent flow they show strong differences in the descent style, as shown in the previous section. This leads to severe differences in the projected frontal area, as can be observed in table 5 from the change in the particle nutation

	N						
a/D	4	5	6	7	8	9	10
0.03	2048	2050	2041	2136	2173	2228	2234
0.05	2091	2156	2206	2277	2245	2329	2360
0.1	2279	2314	2399	2496	2473	2448	2546
0.15	2441	2513	2665	2632	2738	2794	2878
0.2	2540	2716	2725	2784	2893	3088	3165

Table 4: Particle Reynolds number (Re) based on the diameter of the circumscribed disk and descent velocity.

angle, θ. Thus, this definition of the drag coefficient, can be understood as a measure of how efficient these geometries are to descend. Here, the Drag Coefficient based on the projected area is obtained as

$$C_D = \frac{2m_{eff}g}{A_p V_z^2} \tag{1}$$

where $m_{eff} = m_p - \rho V$ is the apparent weight (buoyancy balanced) measured prior to the experiments, g is the gravity, V_z is obtained as the mean descent velocity for all particle realizations and A_p is the area of the particle projected to the descent direction. Since the disk is used as a reference particle, the Drag Coefficient of the disk is used to make this parameter dimensionless. Figure 7 b) shows the variation in Drag Coefficient ($\widehat{C_D} = \frac{C_{D_p}}{C_{D_d}}$) as a function of the particle number of peaks (N). The variation in the Drag Coefficient across the entire range of particle geometries becomes more pronounced as the a/D ratio increases, maintaining the trends discussed in the particle descent velocity.

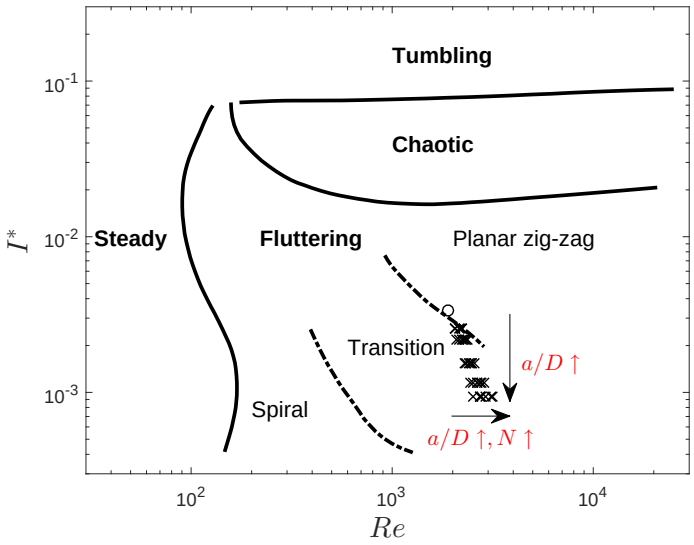

Figure 6: Phase diagram spanned by I^* and Re. Solid lines correspond to the diagram originally defined in Field et al. (1997) and broken lines to the subregimes found in Zhong et al. (2011). The circle corresponds to the disk ($Re \approx 1800$, $I^* \approx 3.4103$) and the crosses to the disk-like particles in the present work.

We believe that small a/D ratios are capable of changing the scale, and hence the lifetime of the turbulent structures present in the wake of disks, reducing the suction effect over the top surface of the particle and therefore increasing the particle descent velocity. In contrast, particles with large a/D ratios and small number of peaks ($N = 4$) tend to move in the $X - Y$ plane with a given peak facing the planar motion, with a pair of peaks to each side at almost 90° with respect to the incoming flow, as shown in figure 8. This configuration clearly favours lift production and therefore the particle descent velocity is reduced. As the number of peaks around the perimeter increases this particle-incoming flow configuration is gradually lost. We be-

	N						
a/D	4	5	6	7	8	9	10
0.03	36	36	36	35	34	35	33
0.05	36	35	35	34	35	34	33
0.1	31	31	30	30	30	30	30
0.15	27	27	26	26	22	23	22
0.2	27	26	22	20	16	11	11

Table 5: Mean of the local maxima of the nutation angle, θ, of the particles during the fall. θ in degrees.

lieve that the increase in the number of large peaks around the perimeter leads to the formation and shedding of complex vortical structures around the periphery of the particle with no preferential configuration. Thus, the particle descends following a more stable path with small inclination angles relative to the descent direction, an almost uniform descent velocity and a severe reduction of the $X - Y$ footprint. This tendency can be observed in the Drag Coefficient ratio plotted in figure 7 b), where particles belonging to the $a/D = 0.2$ family exhibit a strong drag reduction as N increases, exceeding the reduction observed all other particles for $N > 8$.

Figure 9 a) depicts the evolution of the instantaneous descent velocity (v_z) of planar particles with the same number of peaks ($N = 10$) but increasing the amplitude of the peaks from $a/D = 0.03$ to $a/D = 0.2$. The differences observed in the peak to peak velocity for individual trajectories in figure 9

a) b)

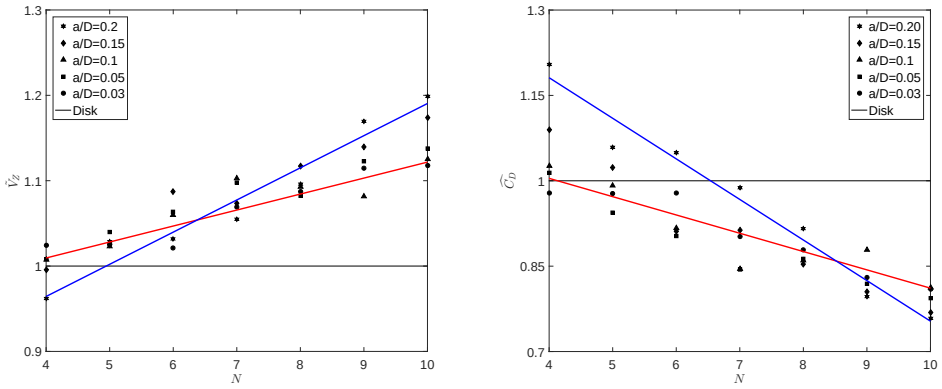

Figure 7: a) Relative mean descent velocity and b) Drag Coefficient ratio ($\widehat{C_D}$) based on the mean descent velocity (V_z) and particle projected area (A_p). Red and blue fitted lines show the trends for the particles belonging to the families of most ($a/D = 0.03$) and least ($a/D = 0.2$) circular particles respectively.

a) are consistent for all realizations, and this can be seen in the standard deviation of the descent velocity for all individual trajectories detailed in figure 9 b). The standard deviation of the descent velocity of each trajectory is obtained from the trajectory section corresponding to 7 D from the release point to 2 D from the bottom. Then, a unique value of the standard deviation per particle geometry is obtained as the mean of the 50 realizations. The standard deviation of the descent velocity is shown relative to the measured for the disk ($\tilde{\sigma}_{V_z} = \sigma_{V_z}/\sigma_{V_z disk}$). The standard deviation of the descent velocity for particles with small a/D is marginally higher than the one found for disks. This is also consistent with the values shown for the mean descent velocity; both of these families show mostly quasi planar zig-zag motion with slow and fast events (as in figure 4 a)) but with a higher mean descent

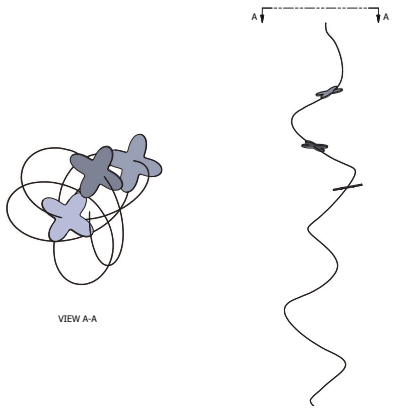

Figure 8: Sketch of a reconstructed 3D trajectory of a $N = 4$, $a/D = 0.2$ particle at three different locations during the fall. The sketch illustrates the particle describing a wide helical fall with a given peak orientated towards the $X - Y$ particle motion.

velocity and therefore we also expect the oscillations about the mean to be stronger. In contrast, for $a/D > 0.1$ the descent style resembles more to the rhodonea curve shown in figure 5 b) with a descent becoming more steady as both a/D and N increases. Interestingly, for families of particles with $a/D > 0.1$ the standard deviation of particles with $N = 4$ becomes smaller as the former ratio increases. We observe a change in the descent style for these four-peaks particles, which describe also a spiral-like paths but with greater $X - Y$ footprint than for the case of high N number. We believe these particles represent a special geometry case, for which the production of lift dominates the settling dynamics.

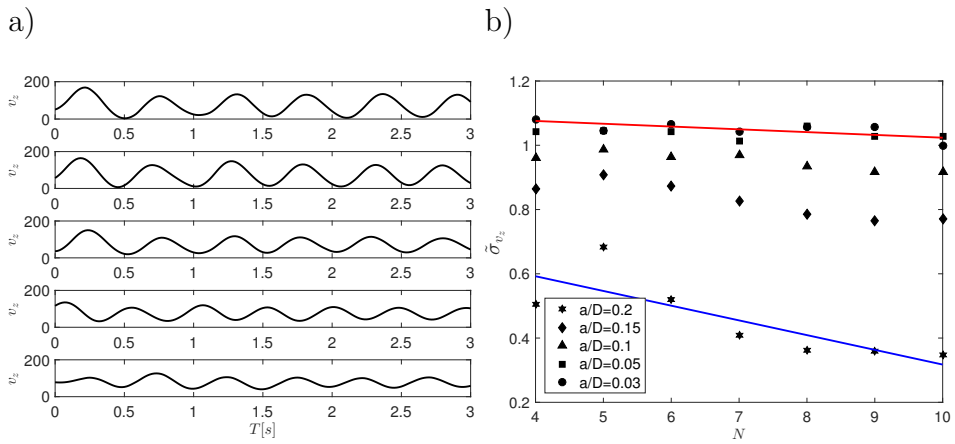

Figure 9: a) Evolution of the descent velocity of different particles with N=10 during specific realizations. From top to bottom: $a/D = 0.03$, $a/D = 0.05$, $a/D = 0.1$, $a/D = 0.15$ and $a/D = 0.2$. b) Standard deviation of the descent velocity along individual trajectories of all particles tested relative to the reference disk.

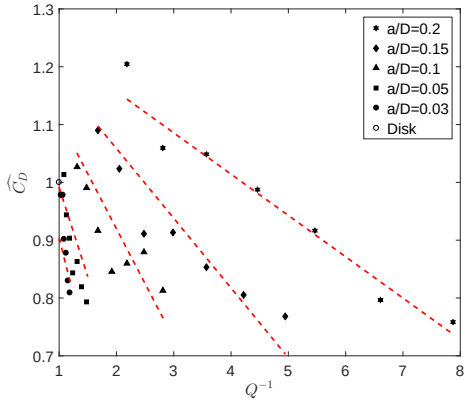

Figure 10: Drag coefficient relative to the reference particle based on the mean projected area during descent as a function of the isoperimetric quotient Q and relative peak amplitude a/D. Broken lines are fitted to the experimetal data of particles belonging to each a/D family following equation 2.

4. Vertical Drag correction for planar irregular particles

There are a large number of empirical correlations for predicting the drag coefficient of non-spherical particles associated with different ranges of validity and accuracy in the literature, as in Bagheri and Bonadonna (2016), Mando and Rosendahl (2010), Holzer and Sommerfeld (2008), Loth (2008), Cong et al. (2004), Leith (1987) and Haider and Levenspiel (1983) among others. However, in most studies the shape descriptor used to characterize particles is the sphericity. Sphericity ψ is defined as the ratio of surface area of a sphere with equivalent volume as the particle to the true surface area of the particle, $\psi = \pi d_{eq}^2 / A_p$. As a result, particles with very different geometry can have the same value of sphericity, and this is in fact what occurs for all particles in this study, therefore the need of an alternative empirical correlation to characterize the settling dynamics of these particles. Although the isoperimetric quotient has a non-unique value for the particles in this study, particles with the same a/D ratio do not have the same isoperimetric magnitude. Therefore, Q is used for the aforementioned purpose. As described in the previous sections, the geometry of the perimeter of planar irregular particles is directly linked to differences in the particle falling style and Drag Coefficient. In figure 10, the mean Drag Coefficient relative to the equivalent disk $\widehat{C_D}$ is shown as a function of the particle circularity (here defined by the isoperimetric quotient Q) and the relative amplitude of the peaks (a/D). Experimental data of particles belonging to different a/D families show distinctive linear trends as the isoperimetric quotient decreases. These trends are represented with straight lines on the $\widehat{C_D} - Q^{-1}$ domain, defined by equation 2, where the slope of the linear trends is defined as a function of

the relative amplitude of the peaks (a/D).

$$\widehat{C_D} = m(a/D)Q^{-1} + 1.3 \tag{2}$$

where $m(a/D)$ is defined as

$$m(a/D) = 0.204 + 0.17\log(a/D) \tag{3}$$

Thus, the mean Drag Coefficient of a planar irregular particle relative to the equivalent disk can be approximated once the a/D ratio and the isoperimetric quotient Q are known.

Similarly, the fluctuations of the Drag Coefficient can be also captured by considering the complete range of values of the particle descent velocity along trajectories. Thus, one can predict the particle behaviour using the mean descent velocity ($\tilde{V_z}$) and the standard deviation of the descent velocity ($\tilde{\sigma}_{vz}$) from figures 7 b) and 9 b) to construct quasi-periodic signals.

5. Conclusions

This work investigated the effect of the particle edge waviness on the free falling motion of planar particles. The reference particle was chosen to be a circular disk that is known to exhibit a 'planar zig-zag' motion (for the $Re - I^*$ values chosen). The Galileo number of the different planar particles was held a constant and the isoperimetric quotient (a measure of particle circularity) was varied by altering edge waviness of the particle to different wave amplitude (a/D) and number of oscillations (N) around the perimeter.

Disks and other disk-like families of particles with small a/D ratios were found to describe 'planar zig-zag' trajectories most of the time and this agrees

well with their location on the $Re - I^*$ regime map. This planar motion is characterised by a gliding phase followed by a turning phase. Particles belonging to families with large a/D ratios but only a few peaks ($N = 4$ and 5) also show a strong tendency to glide but with a given peak facing the horizontal motion. The pair of peaks to each side are at almost 90^o with respect to the incoming flow, clearly favouring lift production and therefore the particle descent velocity is reduced.

As the number of peaks around the perimeter increases the lift production configuration is gradually lost. We believe that the presence of large peaks around the perimeter leads the formation and shedding of complex turbulent structures around the periphery of the particle with no preferential configuration. Thus, the particle descends following a more stable path with small inclination angles relative to the descent direction, an almost uniform descent velocity and a severe reduction of the $X - Y$ footprint. It is important to mention that although these trajectories appear to be qualitatively similar to the ones observed for disks with low inertia, as in Lee et al. (2013), the vortex shedding mechanisms might severely differ. While long helical vortices are shed continuously from the disk edge, we expect to observe a more complex wake behind these irregular particles that might reduce lift production and therefore enhance particle descent.

These falling styles are shown to be directly linked to the particle radial distribution, mean descent velocity and Drag Coefficient. The radial distribution of particles from the same a/D family collapses when the particle perimeter and isoperimetric quotient are used to make particle dispersion non-dimensional. On the other hand, Drag Coefficient based on the projected

area of planar particles reduces with reducing the isoperimetric quotient for any given a/D family of particles, with the family $a/D = 0.2$ having more than 15% speed-specific drag reduction for $N = 9$ and 10.

We propose an empirical correlation for the mean Drag Coefficient of these particles based on the isoperimetric quotient (Q) and the relative amplitude of the peaks around the perimeter (a/D) and show that the fluctuations in drag are well captured using normal distribution functions.

We believe that with information such as this, it is possible to simulate the vertical trajectory content of these particles using Monte Carlo type simulations with Lagrangian points, as discussed in Zastawny et al. (2012), and also that this same approach can be used to obtain a prediction of the speed-specific drag and drag coefficient of any planar irregular particle whose equivalent disk lies in the fluttering region. Similarly, data from the particle radial dispersion can also be used to predict the $X - Y$ particle behaviour during the descent.

6. Acknowledgments

This work was supported by Aquavitrum Ltd., the Leverhulme Trust and the Faculty of Engineering and Physical Sciences of University of Southampton. Pertinent data for this paper are available at https://doi.org/10.5258/SOTON/D0652.

References

Andersen, A., Pesavento, U., Wang, Z. J., 2005a. Analysis of transitions between fluttering, tumbling and steady descent of falling cards. J. Fluid Mech 541, 91–104.

Andersen, A., Pesavento, U., Wang, Z. J., 2005b. Unsteady aerodynamics of fluttering and tumbling plates. J. Fluid Mech 541, 65–90.

Auguste, F., Magnaudet, J., Fabre, D., 2013. Falling styles of disks. J. Fluid Mech. 719, 388–405.

Bagheri, G. H., Bonadonna, C., 2016. On the drag of freely falling non-spherical particles. Powder Technology 301, 526–544.

Belmonte, A., Eisenberg, H., Moses, E., 1998. From flutter to tumble: intertial drag and froude similarity in falling paper. Phys. Rev. Lett. 81, 345–348.

Chrust, M., Bouchet, G., Dusek, J., 2013. Numerical simulation of the dynamics of freely falling discs. Physics of Fluids 25, 044102.

Cong, S. T., Gay, M., Michaelides, E. E., 2004. Drag coefficients of irregular shaped particles. Powder Technology 139, 21–32.

Esteban, L. B., Shrimpton, J., Ganapathisubramani, B., 2018. Edge effects on the fluttering characteristics of freely falling planar particles. Phys. Rev. Fluids 3, 064302.

Field, S. B., Klaus, M., Moore, M. G., Nori, F., 1997. Chaotic dynamics of falling disks. Nature 388, 252–254.

Haider, A., Levenspiel, O., 1983. Drag coefficient and terminal velocity of spherical of non-spherical solid particles. Powder Technology 58, 63–70.

Heisinger, L., Newton, P., Kanso, E., 2014. Coins falling in water. J. Fluid Mech. 714, 243–253.

Holzer, A., Sommerfeld, M., 2008. New simple correlation formula for the drag coefficient of non-spherical particle. Powder Technology 184, 361–365.

Jayaweera, K. O. L. F., 1972. An equivalent disc for calculating the terminal velocities of plate-like ice crystals. J. Atmos. Sci. 29, 596–597.

Kajikawa, M., 1992. Observations of the falling motion of plate-like crystals. part i: The free-fall patterns and velocity variations of unrimed crystals. J. Meteor. Soc. Japan 70, 1–9.

Lee, C., Su, Z., Zhong, H., Chen, S., Zhou, M., Wu., J., 2013. Experimental investigation of freely falling thin disks. part 2. transition of three-dimensional motion from zigzag to spiral. J. Fluid Mech. 42, 77–104.

Leith, D., 1987. Drag on nonspherical objects. Aerosol Science and Technology 6, 153–161.

List, R., Schemenauer, R. S., 1971. Free-fall behaviour of planar snow crystals, conical graupel and small hail. J. Atmos. Sci. 28, 110–115.

Loth, E., 2008. Drag of non-spherical solid particles of regular and irregular shape. Powder Technology 182, 342–353.

Maggi, F., 2015. Experimental evidence of how the fractal structure controls the hydrodynamic resistance on granular aggregates moving through water. J. Hydrology 528, 694–702.

Mando, M., Rosendahl, L., 2010. On the motion of non-spherical particles at high reynolds number. Powder Technology 202, 1–13.

Moffatt, H. K., 2013. Three coins in a fountain. J. Fluid Mech. 720, 1–4.

Vincent, L., Shambaugh, W. S., Kanso, E., 2016. Holes stabilize freely falling coins. J.Fluid Mech. 801, 250–259.

Willmarth, W. W., Hawk, N. E., Harvey, R. L., 1964. Steady and unsteady motions and wakes of freely falling disks. Phys. Fluids 7, 197–208.

Zastawny, M., Mallouppas, G., Zhao, F., van Wachem, B., 2012. Derivation of drag and lift force and torque coefficients for non-spherical particles in flows. Int. J. Multiphase Flow 39, 227–239.

Zhong, H., Chen, S., Lee, C., 2011. Experimental study of freely falling thin disks: Transition from planar zigzag to spiral. Physics of Fluids. 23, 011702.

Zhou, W., Chrust, M., Duek, J., 2017. Path instabilities of oblate spheroids. J. Fluid Mech. 833, 445–468.